J. Fluid Mech. (2012), *vol.* 710, *pp.* 5–34.
doi:10.1017/jfm.2012.324

Turbulent boundary layers at moderate Reynolds numbers: inflow length and tripping effects

Philipp Schlatter† and Ramis Örlü

Linné FLOW Centre and Swedish e-Science Research Centre (SeRC), KTH Mechanics, SE-100 44 Stockholm, Sweden

(Received 18 December 2011; revised 29 April 2012; accepted 23 June 2012; first published online 21 August 2012)

A recent assessment of available direct numerical simulation (DNS) data from turbulent boundary layer flows (Schlatter & Örlü, *J. Fluid Mech.*, vol. 659, 2010, pp. 116–126) showed surprisingly large differences not only in the skin friction coefficient or shape factor, but also in their predictions of mean and fluctuation profiles far into the sublayer. While such differences are expected at very low Reynolds numbers and/or the immediate vicinity of the inflow or tripping region, it remains unclear whether inflow and tripping effects explain the differences observed even at moderate Reynolds numbers. This question is systematically addressed by re-simulating the DNS of a zero-pressure-gradient turbulent boundary layer flow by Schlatter *et al.* (*Phys. Fluids*, vol. 21, 2009, art. 051702). The previous DNS serves as the baseline simulation, and the new DNS with a range of physically different inflow conditions and tripping effects are carefully compared. The downstream evolution of integral quantities as well as mean and fluctuation profiles is analysed, and the results show that different inflow conditions and tripping effects do indeed explain most of the differences observed when comparing available DNS at low Reynolds number. It is further found that, if transition is initiated inside the boundary layer at a low enough Reynolds number (based on the momentum-loss thickness) $Re_\theta < 300$, all quantities agree well for both inner and outer layer for $Re_\theta > 2000$. This result gives a lower limit for meaningful comparisons between numerical and/or wind tunnel experiments, assuming that the flow was not severely over- or understimulated. It is further shown that even profiles of the wall-normal velocity fluctuations and Reynolds shear stress collapse for higher Re_θ irrespective of the upstream conditions. In addition, the overshoot in the total shear stress within the sublayer observed in the DNS of Wu & Moin (*Phys. Fluids*, vol. 22, 2010, art. 085105) has been identified as a feature of transitional boundary layers.

Key words: transition to turbulence, turbulent boundary layers, turbulence simulation

1. Introduction and motivation

Since the first resolved direct numerical simulation (DNS) of turbulent channel flows became available (Kim, Moin & Moser 1987) more than two decades ago, a large number of DNS have been performed for various flow cases, from canonical geometries (channels, boundary layers, pipes) to more complex ones. Mainly for

† Email address for correspondence: pschlatt@mech.kth.se

canonical geometries, the Reynolds number (Re) extent of the available simulation data has constantly been increasing, finally reaching those ranges covered by well-resolved (and well-controlled) experiments. In particular, channel flow has become the prime area for simulations, given its geometrical simplicity and the ease of specifying boundary conditions (periodicity). Hence, it was not surprising that a detailed comparison between DNS and corresponding experiments in a (fully developed) turbulent channel flow showed generally good agreement for the first- and second-order moments as well as spectral distributions of the streamwise velocity component (Monty & Chong 2009).

Although zero-pressure-gradient (ZPG) turbulent boundary layers (TBLs) have been simulated extensively beginning with Spalart (1988*b*), DNS of truly spatially developing TBLs have only recently become feasible that reach Reynolds numbers comparable to those of DNS from moderate-Re channel flows (Skote, Haritonidis & Henningson 2002). Furthermore, the recent comparison by Schlatter & Örlü (2010) of published DNS data from ZPG TBL flows has revealed that there exists considerable scatter between the various data sets even in basic integral quantities, e.g. up to 5 % and 20 % in the shape factor H_{12} and skin friction coefficient c_f, respectively. First- and second-order velocity statistics not only differed within the wake region, but throughout the entire boundary layer far into the buffer region. In that study it was observed that various groups use slightly different definitions and methods to evaluate boundary-layer quantities, therefore all data were re-evaluated based on a uniform approach. Here, some of these previous comparisons are reproduced in order to set the stage for the forthcoming comparisons. Note that the database has been updated with the two new simulations by Wu & Moin (2010) and Lee & Sung (2011). In figure 1 the shape factor H_{12} and the ratio of boundary-layer thicknesses as a measure of the outer flow development are shown, while in figure 2 the skin-friction coefficient c_f and the magnitude of the fluctuating wall shear stress $\tau^+_{w,rms}$ to characterize the near-wall region are depicted. In particular the shape factor can be regarded as a good scalar indicator of the state of a ZPG boundary layer (Chauhan *et al.* 2009). The complete references for the data used and the corresponding symbols are listed in table 1. From the two figures it becomes obvious that considerable discrepancies exist: some of these differences are seemingly related to inflow effects as the spread appears to decrease with increasing streamwise coordinate in each simulation box (e.g. for H_{12} or c_f). Other differences however are more systematic, as evidenced by the fluctuating wall shear stress, $\tau^+_{w,rms}$. Probably the most sensitive quantities when it comes to an assessment of the region very close to turbulence transition (i.e. low Reynolds numbers) are the ratios of integral boundary-layer thicknesses, such as the displacement (δ_*) and momentum-loss (θ) thicknesses, to the 99 % boundary-layer thickness, δ_{99}. The various DNS exhibit a large scatter at lower Reynolds numbers which is clearly related to the different ways the flow is being brought through transition.

Despite these differences between various DNS databases in general, and specifically at low Reynolds numbers, a good agreement between a recent large-scale DNS and an experiment with a similar setup and boundary conditions at $Re_\theta \approx 2500$ has been reported in Schlatter *et al.* (2009). Hence, there is a need to address why integral quantities as well as higher-order turbulence statistics between various DNS of the same flow differ substantially, even beyond the aforementioned Reynolds number at which the good agreement between experiment and DNS was documented (Schlatter *et al.* 2009). Some of the main possible candidates responsible for the discrepancies have already been conjectured in Schlatter & Örlü (2010), such as the inflow

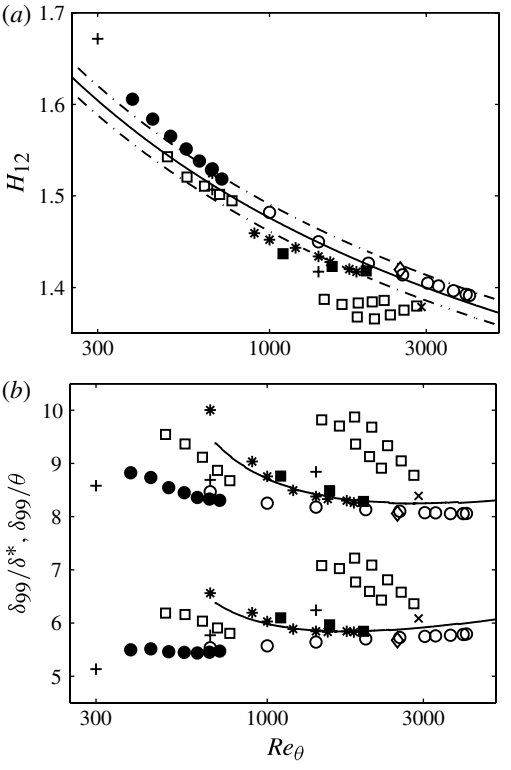

FIGURE 1. Ratios of boundary-layer thicknesses, extracted from various literature DNS data as a function of Reynolds number. (*a*) Shape factor, $H_{12} = \delta^*/\theta$. The solid line represents integration of the composite profile by Chauhan, Monkewitz & Nagib (2009) including an ad-hoc low-*Re* correction (cf. equation (8) in Chauhan *et al.* 2009), while the dash-dotted lines indicate a 1 % tolerance. (*b*) Displacement thickness, δ^*, and momentum-loss thickness, θ, over boundary layer thickness, δ_{99}. The integral quantities from the various DNS profiles as well as the solid lines in (*b*), which represent results from the composite profile (Chauhan *et al.* 2009), are evaluated in a consistent manner by following the scheme outlined in Schlatter & Örlü (2010). Symbols according to table 1.

Reynolds number and turbulence generation method, the settling length to reach a final developed turbulent state, as well as box dimensions, boundary conditions and residual pressure gradients. However, simulation resolution is probably of lesser importance, as all the DNS included in the comparison can be considered well-resolved according to present standards.

To what extent the differences due to the aforementioned causes persist in statistical quantities and whether the outer layer actually completely forgets its initial or upstream conditions and thus converges (or tends within the investigated *Re*-range) to an asymptotic state has been the focus of various studies dating back to Klebanoff & Diehl (1954). These authors investigated experimentally a boundary layer that was tripped to turbulence. They found that a fully developed TBL could be achieved essentially free from any distortions introduced by the tripping process, i.e. independent of its initial conditions, beyond a certain development length depending on the tripping device itself. However, the question regarding the quantification of a sufficient development length and the appropriate tripping

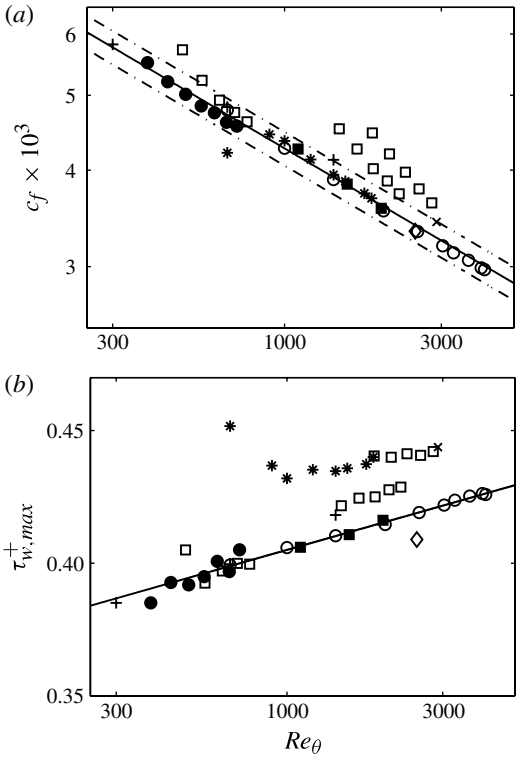

FIGURE 2. (*a*) Skin friction coefficient, c_f, as a function of Reynolds number. Solid line represents the correlation by Smits, Matheson & Joubert (1983) and dash-dotted lines indicate a 5 % tolerance. (*b*) Fluctuating wall shear stress, $\tau^+_{w,rms}$, as a function of Reynolds number. Solid line represents correlation given in Schlatter & Örlü (2010), i.e. $\tau^+_{w,rms} = 0.298 + 0.018 \ln Re_\tau$. Symbols according to table 1.

method still remains open today as emphasized in the recent review article by Marusic *et al.* (2010). When it comes to the Reynolds shear stress or the wall-normal Reynolds normal stress, it has even been questioned whether there exists an asymptotic state independent of upstream conditions at all, as highlighted by Castillo & Johansson (2002) and Seo *et al.* (2004).

It is interesting to recall that the classical assessment of experimental data sets by Coles (1954) states that 'it is not obvious *a priori* that a state is ever reached in which the dependence of the turbulent boundary layer on its early history is no longer measurable in terms of the local mean properties of the flow'. Similarly, the review on ZPG TBL flows by Fernholz & Finley (1996) identifies the tripping devices as an important secondary factor that might explain differences between various (experimental) data sets, while a more recent re-assessment of experimental data from ZPG TBL flows by Chauhan *et al.* (2009) lists 'three major local experimental conditions existing in the tunnel for various data sets, i.e. an insufficient or excessive transition trigger, a history of pressure-gradient and inadequate development length' as possible causes for differences in the outer part of the mean flow. One reason why apparent differences between past and present experimental data sets could not solely be traced back to initial or upstream conditions (in contrast to measurement-technique-related shortcomings) is the 'fact that in many experiments these effects (i.e. the initial

Reference/Label	Re_θ	Method	Symbol
Spalart (1988*b*)	300, 600, 1410	Spectral Spatio-temporal	+
Komminaho & Skote (2002)	383−716	Spectral Tripping at $Re_\theta \approx 200$ Domain up to $Re_\theta \approx 750$	●
Khujadze & Oberlack (2004, 2007)	489−2807	Spectral Tripping close to respectively inflow Domain length $\Delta Re_\theta \approx 500$	□
Ferrante & Elghobashi (2005)	2900	Finite differences Rescaling and recycling Domain $Re_\theta = 2340$–2900	×
Simens *et al.* (2009)	1000, 1550, 1968	Finite-difference/spectral Rescaling and recycling Domain $Re_\theta = 620$–2140	■
Wu & Moin (2010)	80−1950	Finite differences second order Free-stream disturbances Laminar inflow at $Re_\theta = 80$	*
Lee & Sung (2011)	2500	Finite differences second order Rescaling and recycling Domain $Re_\theta = 570$–2560	◇
All of the following simulations were performed in a *single domain* using a *spectral method*			
Schlatter *et al.* (2009) 'Baseline'	180−2500	Tripping at $Re_\theta = 180$ Optimized tripping parameters	—— (blue)
Schlatter & Örlü (2010)	180−4300	Tripping at $Re_\theta = 180$ Lower amplitude compared to above	– – – (blue) ○
LA	180−2400	Low-amplitude tripping at $Re_\theta = 180$	– – – (green)
TS	180−2000	Tollmien–Schlichting waves ($F = 120$)	—— (green)
LF	180−2100	Low frequency tripping at $Re_\theta = 180$	– – – (red)
HF	180−2500	High frequency tripping at $Re_\theta = 180$	—— (red)
LR	55−2000	Tripping at $Re_\theta = 55$, LES	- - - - - (black)
HR	750−2900	Tripping at $Re_\theta = 750$, LES	- – - – - (black)

TABLE 1. List of employed DNS data, their Reynolds-number ranges and the key characteristics of the turbulence generation mechanism. If more than three profiles have been used from a given reference, only the range of Reynolds numbers is given.

or upstream conditions) are not, or only incompletely, documented' (Marusic *et al.* 2010), a fact that is mainly related to the elaborate work associated with quantifying the full set of initial and upstream conditions in experiments. A notable exception in this respect is the seminal work by Erm & Joubert (1991) who studied the effect of different tripping devices for various free-stream velocities on the evolution of integral quantities such as shape factor, skin friction and wake parameter, as well as profiles of mean and various fluctuating components. While their Reynolds numbers for obtaining turbulent boundary layers were as low as $Re_\theta = 509$–581 depending on tripping devices, the authors concluded that independent of tripping device an overall agreement (mainly presented in outer scaling) could be reached for $Re_\theta > 2175$.

In the framework of the present study, the influence of varying upstream conditions is studied in a systematic way. The previous DNS of a ZPG TBL flow by Schlatter *et al.* (2009) serves as the baseline simulation, as it has been already demonstrated that accurate comparisons with experiments could be achieved at $Re_\theta = 2500$ given the particular upstream parameters. We thus proceed by re-simulating that DNS, however with physically different upstream conditions, i.e. by varying the tripping parameters (amplitude, frequency etc.), and the inflow Reynolds number (i.e. the location of the tripping). In that sense, the present investigation can be seen as a direct continuation of Schlatter & Örlü (2010), since it enables the direct assessment of various turbulence generation mechanisms and the possibility to define various measures to discern the starting point from which a ZPG TBL flow can be considered independent of its upstream history. Although Jiménez *et al.* (2008) and Simens *et al.* (2009) investigated the effect of turbulent inflow conditions specifically for their DNS of a ZPG TBL, their conclusion, i.e. that a distance of at least 300 initial momentum-loss thicknesses has to be passed before the effect of the artificial inflow is forgotten, is not necessarily of a general nature, but rather specific to the employed recycling method. Note in this respect also that a recent large-scale DNS by Sillero *et al.* (2011) reaching the higher $Re_\theta = 6650$, starting with a series of auxiliary simulation domains for the generation of proper inflow conditions, appears to reach fully developed conditions only towards the end of the simulation box. This shows that the required inflow length is actually larger than previously expected, indicating a Reynolds-number dependence. The present work, on the other hand, can more closely be related to systematic wind tunnel experiments, in which the flow undergoes forced laminar–turbulent transition and various tripping devices are tested by studying the downstream evolution of the boundary layer. In this respect it can be seen as the numerical counterpart of the study by Erm & Joubert (1991) with the advantage of having access to the full characteristics of initial and upstream conditions (which is rarely accomplished in experiments; see Marusic *et al.* 2010). We therefore focus in this study on tripping mechanisms and corresponding parameters likely to be found in experiments, thereby excluding boundary-layer receptivity to free-stream disturbances (see e.g. Brandt, Schlatter & Henningson 2004). To the authors' knowledge there is no previous study investigating the effects of different turbulence generation mechanisms, i.e. inflow length and tripping effects, in spatially developing flows, so the current investigation is especially significant in this respect.

The present paper will conclude that different inflow conditions and residual tripping effects do indeed explain most of the differences observed when comparing available DNS data. It will also be shown that if transition is initiated at a low enough Reynolds number (based on the momentum-loss thickness) $Re_\theta < 300$, all quantities agree well for both inner and outer layer for $Re_\theta > 2000$. Also, a previously observed overshoot in the total shear stress within the sublayer observed in the DNS of Wu (2010) up

to $Re_\theta = 1900$ (see also Wu & Moin 2009*a*, 2010) has been identified as a feature of transitional boundary layers. Based on these results a lower limit for a meaningful comparison between numerical and/or wind tunnel experiments can be established, i.e. $Re_\theta > 2000$.

The paper is organized as follows. In § 2 the simulation approach is briefly introduced together with a quantification of the tripping parameters. The comparisons between the various cases is given in § 3 for integral quantities, mean flow, Reynolds normal and shear stresses. Finally, § 4 summarizes the present findings and ends with practical guidelines.

2. Existing and new direct numerical simulations

In this paper numerical simulations of turbulent boundary layers developing in the downstream direction on top of a smooth wall are considered. The inflow is laminar Blasius flow. Transition to turbulence is induced a short distance downstream of the inlet via a volume force (*trip forcing*) acting in the near-wall region. Therefore, all our cases induce transition and turbulence from the wall; free-stream disturbances and the corresponding receptivity processes are therefore not considered. Wall-induced transition is, however, close to experimental setups in wind tunnels, and thus especially relevant. Furthermore, we chose to model a real tripping device (such as roughness, vibrating ribbons etc.) using a volume force as described below; this approximation is assumed to not influence the flow development further downstream of the tripping location. For the main part of the present investigation the DNS of a ZPG TBL by Schlatter *et al.* (2009), here serving as the baseline simulation, was re-simulated, however with different tripping parameters to examine these effects on the turbulent boundary layer developing downstream. In particular, simulations with a lower tripping amplitude (LA), lower (LF) and higher (HF) tripping frequency, and 'classical transition' via exponential growth of Tollmien–Schlichting (TS) waves were considered as the turbulence-generation mechanisms. Additionally, a simulation with tripping at a considerably higher *Re* (HR) was considered, since this is a common way to reach cost-efficiently a high Reynolds number (Khujadze & Oberlack 2007), and finally one with tripping at a considerably lower *Re* (LR), similar to Wu & Moin (2010). In the following two subsections a brief description of the numerical method and the exact details of the formulation of the trip forcings is given. Finally, in § 2.3 visualizations of the flow are provided in order to appreciate the structural differences during transition due to the various tripping parameters.

2.1. *Numerical method*

All the present simulations are performed using a fully spectral method to solve the time-dependent, incompressible Navier–Stokes equations (Chevalier *et al.* 2007). In the wall-parallel directions, Fourier series with full dealiasing are used whereas the wall-normal direction is discretized with Chebyshev polynomials. Periodic boundary conditions in the streamwise direction are combined with a spatially developing boundary layer by adding a 'fringe region' at the end of the domain; similar techniques have already been employed by Spalart (1988*a*) and Bertolotti, Herbert & Spalart (1992). In this region, the governing Navier–Stokes equations are augmented by a linear forcing which reduces the fluctuation level in the layer, and causes vertical inflow in order to reduce the boundary-layer thickness. In consequence, the flow at the inlet ($x = 0$) is laminar Blasius flow at the specified inlet Reynolds number, free

from any disturbances from the downstream end of the physical domain (Nordström, Nordin & Henningson 1999). Note that a truly spatially developing boundary layer is simulated, and the fringe region is purely a numerical method to achieve this with high accuracy compatible with Fourier discretization. For further details on the exact simulation setup the reader is referred to Schlatter *et al.* (2009).

The various runs in this study are summarized in table 1, together with their Reynolds-number range. The numerical resolution and box dimensions for cases LA, TS, LF and HF are exactly the same as the baseline case (Schlatter *et al.* 2009), i.e. $\Delta x^+ = 12$, $\Delta {y_{max}}^+ = 8.6$, $\Delta z^+ = 6.4$ obtained with a grid of $3072 \times 301 \times 256$ spectral collocation points in the streamwise, wall-normal and spanwise direction, respectively. Cases LR and HR are well-resolved large-eddy simulations (LES), with resolutions similar to the previous LES study by Schlatter *et al.* (2010*c*). In addition to the aforementioned baseline and new simulations, the DNS described by Schlatter & Örlü (2010) over the extended range of $Re_\theta = 180$–4300 is included here as well to indicate the trends beyond the Re-range covered by the new simulations.

2.2. *Numerical tripping*

The tripping is implemented as a weak random volume force acting in the wall-normal direction. The main inputs are amplitude, spanwise length scale and temporal frequency. Although a direct association with a specific shape of an experimental tripping device is impossible, the flow features downstream of the tripping and the corresponding transition mechanisms are expected to resemble what a physical trip would have induced. For instance, it appears natural that the amplitude and the vertical shape of the trip can be associated with the height of a roughness element, whereas the time scales relate to the shedding characteristics of a real trip; similarly the spanwise scale is associated with the physical scales of the trip. Formally, the specific force, entering the Navier–Stokes equations on the right-hand side, is written as

$$F_2 = \exp([(x - x_0)/\ell_x]^2 - [y/\ell_y]^2) g(z, t), \tag{2.1}$$

where the two parameters ℓ_x and ℓ_y denote the spatial Gaussian attenuation of the forcing region. The force thus appears as a Gaussian blob centred around the streamwise position x_0 and the wall ($y = 0$). The actual forcing function $g(z, t)$ is allowed to vary both in time t and the spanwise direction z to be able to impose temporal and spanwise frequencies. The force is composed as follows:

$$g(z, t) = A_t[\{1 - b(t)\}h^i(z) + b(t)h^{i+1}(z)]. \tag{2.2}$$

Here, $b(t) = 3p^2 - 2p^3$, $p = t/t_s - i$ and $i = \mathrm{int}(t/t_s)$ with $\mathrm{int}(\cdot)$ denoting the integer part of the argument. The temporal fluctuations are thus implemented as third-order Lagrange interpolants with time scale t_s (Chevalier *et al.* 2007). The mechanism is illustrated in figure 3(*a*). The time evolution is split into intervals $i = 0, \ldots$ of length t_s, which are characterized by a random value of $h^i(z)$. In between, the value of the function $g(t)$ is interpolated using a third-order polynomial, ensuring continuity in the zeroth- and first-order derivative. The $h^i(z)$ are random harmonic signals with unit amplitude for all wavenumbers below $2\pi/z_s$, and zero amplitude for all waves above $2\pi/z_s$. The shape of the forcing $g(z, t)$ is thus fully described by two parameters, the spanwise scale z_s and the temporal scale t_s. With this specific formulation, the trip forcing is independent of the time step used in a simulation, and, provided that a suitable pseudo-random number generator is used, accurate restarts of a simulation are possible without introducing any errors or discontinuities.

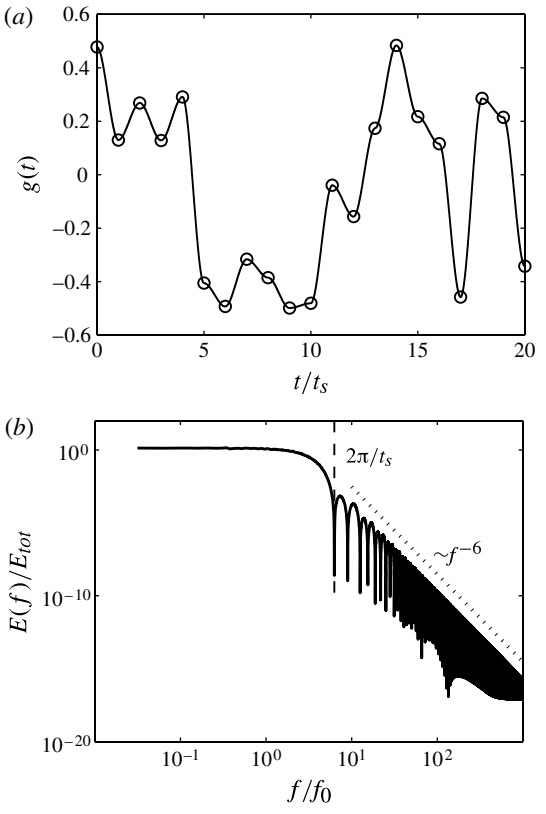

FIGURE 3. (*a*) Sample evolution of tripping function $g(t)$ according to (2.2); symbols indicate the change-over points at times $t = i\,t_s$ for $A_t = 1$. (*b*) Normalized temporal power spectrum of the tripping amplitude. The cutoff time scale is denoted by $t_s = 1$.

In figure 3(*b*), the resulting temporal spectrum is shown; the spectral energy is equipartioned until the temporal cutoff length t_s is reached, which is followed by a steep decrease of the energy $\sim f^{-6}$ towards zero, as a consequence of the third-order polynomial ansatz for g. The trip forcing thus includes fluctuations which are uniformly distributed in both wavenumber and frequency with scales larger than z_s and t_s. For all the cases, the location of the forcing is chosen to be very close to the (laminar) inlet at $x_0 = 10\delta_0^*$ with δ_0^* denoting the displacement thickness of the inflowing laminar Blasius boundary layer. The attenuation length in both streamwise and wall-normal directions is chosen as $\ell_x = 4\delta_0^*$ and $\ell_y = \delta_0^*$. For the baseline case, a temporal cutoff scale $t_s = 4\delta_0^*/U_\infty$ and a spanwise cutoff scale $z_s = 1.7\delta_0^*$ has been chosen. For case LA, the amplitude is reduced to 25 %, in case LF the temporal scale is increased by a factor of 5, and in case HF the frequency is increased by a factor of 4 and z_s is halved. Cases LR and HR use similar scales and amplitudes as the baseline run. In case TS, instead of a random tripping, harmonic disturbances are introduced with non-dimensional frequency $F = 120$, corresponding to a circular frequency of $\omega_0 = 10^{-6} F\, Re_{\delta_0^*}$. This forcing is two-dimensional, i.e. spanwise uniform. In order to trigger secondary instability and subsequent breakdown to turbulence, small-amplitude white noise is also included, superimposed onto the harmonic signal. This type of forcing can be viewed as a numerical counterpart of a vibrating ribbon, inducing

disturbances at a given frequency. More information about this forcing is given in Schlatter *et al.* (2010*b*).

2.3. *Flow visualization*

The disturbances introduced into the flow as discussed in § 2.2 will all lead to laminar–turbulent transition, but following different routes depending on the forcing parameters as apparent from the visualizations given in figure 4. Here, the streamwise development of the flow is shown by means of isocontours of vortical structures, identified by the λ_2 criterion (Jeong & Hussain 1995).

We start our description with the case in which harmonic forcing is applied close to the inlet, case TS, depicted in figure 4(*a*). The non-dimensional frequency F is chosen such that a considerable part of the flow domain is linearly unstable, leading to exponentially growing Tollmien–Schlichting (TS) waves of the same frequency further downstream. Owing to the low-amplitude superimposed white noise, secondary instability is triggered close to Branch II ($Re_x = 590\,000$ based on streamwise distance from the leading edge), which manifests itself in the generation of Λ-shaped vortices, which break down to a localized turbulent spot via the formation of hairpin vortices. Commonly, this transition scenario is referred to as the *classical* route via linearly unstable primary disturbances with subsequent secondary instability. The flow structures during turbulent breakdown are more clearly seen in an enlarged view, figure 5(*a*). The hairpin vortices quickly give rise to a packet of hairpins, forming an incipient turbulent spot. These spots quickly spread and merge, such that a short distance downstream of Branch II the full spanwise extent of the domain is turbulent. Note that the Λ-vortices initially appear in a staggered pattern, being thus of subharmonic (H) type.

The remaining cases, figure 4(*b–g*), are all obtained with varying parameters for the trip forcing as described earlier. For the baseline case, figure 4(*e*), quick transition is induced at approximately the same streamwise distance across the whole span of the flow (*concentrated* breakdown), indicating that the intermittency γ (i.e. the time of the flow being turbulent) quickly rises from zero to unity over a short downstream distance of $\sim 10\delta_0^*$. The transition mechanism is highlighted in figure 5(*c*). The trip forcing induces a comparatively small displacement of the flow in the wall-normal direction. Via the lift-up effect (Landahl 1980), after which a fluid particle initially retains its original momentum when displaced vertically, relatively strong streamwise streaks are quickly formed, which subsequently break down to turbulence via the formation of hairpin vortices (Schlatter *et al.* 2010*a*) on top of low-speed streaks. Similar behaviour is also observed for cases HF, LR, and HR (see visualizations in figure 4*d,f,g*). The latter two cases are characterized by a different Reynolds number at the inlet, and are thus not directly comparable to the other cases. We have also performed an additional simulation in which the trip force only contains the random spanwise variation (with fine spanwise scale as in case HF), but is steady in time (i.e. $t_s \to \infty$). This specific choice of parameters can be thought of as resembling the effect of small-scale roughness. The flow behaviour consists of an initially steady array of streaks, which then quickly breaks down to fully random turbulence in a very similar manner to case HF. Since all characteristics are very similar to case HF we do not further discuss that case.

On the other hand, cases LF and LA (figure 4*b,c*), tend to form incipient turbulent spots (similar to bypass transition caused by free-stream disturbances as e.g. described in Brandt *et al.* 2004), which then grow while travelling downstream and eventually merge to produce a fully turbulent flow. In those cases, the intermittent character of

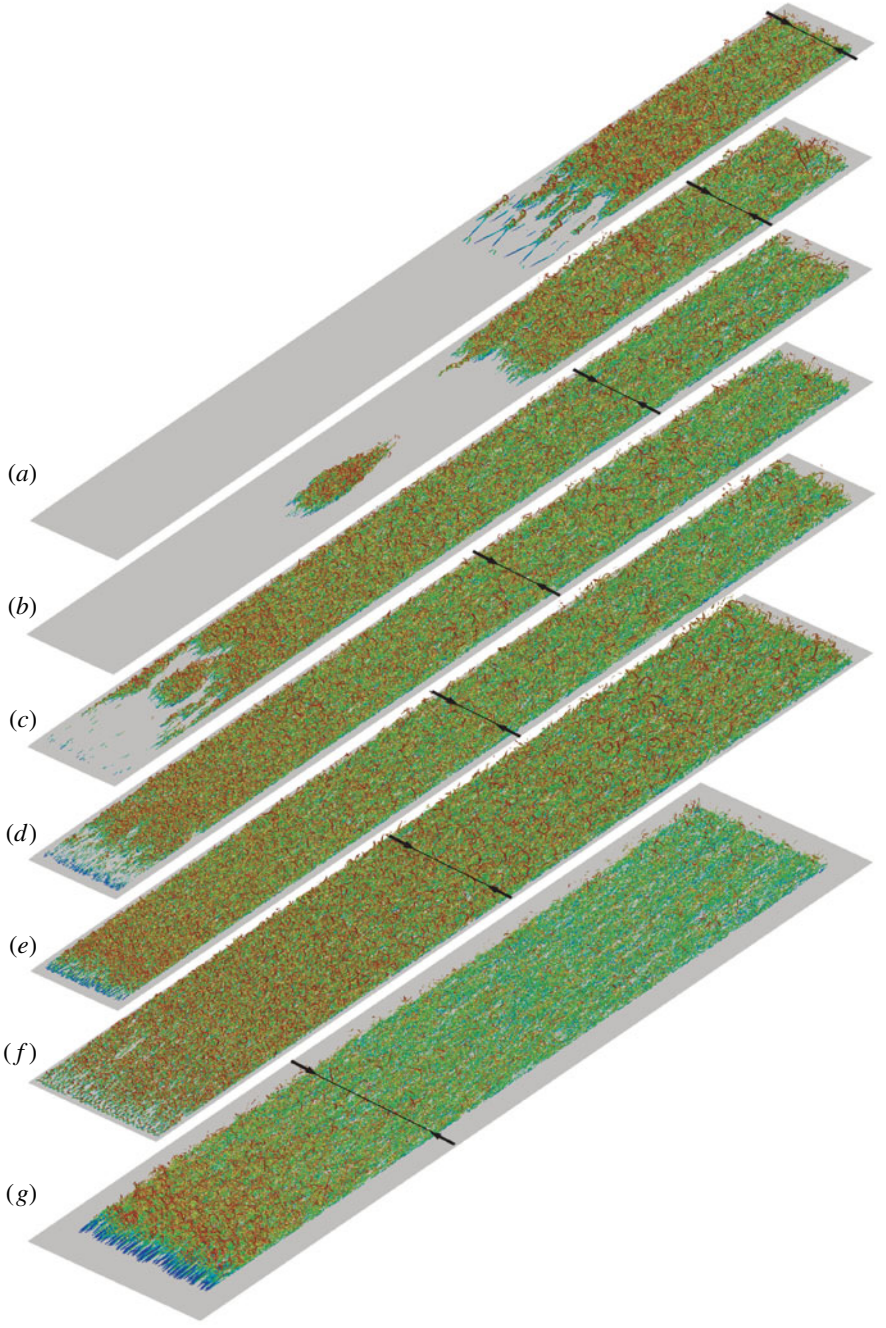

FIGURE 4. Visualization of the streamwise development of vortical structures by means of isocontours of $\lambda_2^+ = -0.005$ (measured at $Re_\theta = 1100$, Jeong & Hussain 1995), coloured with the streamwise velocity, from blue (low) to red (high). The streamwise extent of the computational domain is roughly twice as long as shown. Visualizations correspond to: (*a*) TS; (*b*) LF; (*c*) LA; (*d*) HF; (*e*) baseline (Schlatter *et al.* 2009); (*f*) LR; and (*g*) HR. The respective downstream positions corresponding to $Re_\theta = 1100$ are indicated by the spanwise lines. Flow from left to right.

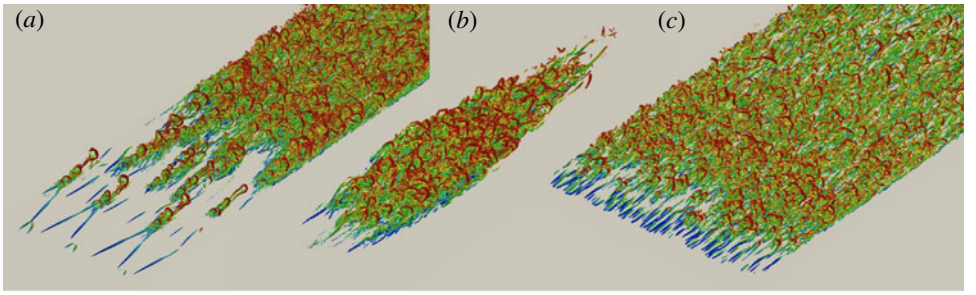

FIGURE 5. Close-up of the transitional flow structures for selected cases: (*a*) TS; (*b*) LF; and (*c*) baseline. Same colour coding and isosurfaces as figure 4.

the flow at low Re_θ becomes evident. Note that the individual turbulent spots share all the characteristics of canonical spots as e.g. described by Emmons (1951), as can be seen from the close-up in figure 5(*b*). In particular the characteristic arrow-head shape, and the overhang region at the downstream end of the spot are clearly visible. Cases LF and LA mainly differ in the frequency of spots, shifting the transition location upstream for case LA.

3. Statistical analysis and discussion

In this section, the results from the various simulations are presented and compared. Starting with integral quantities in § 3.1, inner- and outer-layer convergence of mean and fluctuating components in §§ 3.2–3.3, the section is ended by discussing the more controversial behaviour of Reynolds and total shear stress in § 3.4.

3.1. *Integral and global quantities*

The streamwise development of vortical structures emerging from a low-amplitude tripping mechanism, shown in figure 4, indicates that a considerable portion of the domain is affected by the way the flow is triggered and consequently will yield a different Re_θ at which laminar–turbulent transition is induced and concluded. A direct and overall assessment of the boundary layer development can be obtained through the boundary-layer thickness, δ_{99}, as well as its integral counterparts, i.e. the displacement thickness, δ^*, and momentum-loss thickness, θ. The ratio of the latter two integral quantities, the shape factor H_{12}, as function of Re_θ is depicted in figure 6(*a*) for all utilized simulations and is considered 'a good indicator of the state of a ZPG boundary layer' (Chauhan *et al.* 2009). These quantities have been evaluated in a consistent manner by direct integration of the mean velocity profiles over the entire domain height. Starting from the laminar value of a Blasius boundary layer, $H_{12} \approx 2.59$, the different cases reach a common trend line at around $Re_\theta = 1000$, where the difference between the various simulations is within $\pm 1\,\%$. The scatter further reduces to below $\pm 0.35\,\%$ at around $Re_\theta = 2000$, which is well below the tolerances given by the 'H_{12} criterion' proposed by Chauhan *et al.* (2009) to identify well-developed ZPG TBL flows. The flow case tripped at a high Re (HR) is naturally outside the given margins, and it is interesting to note that even at $Re_\theta = 2500$ it is not only 2 % below the value shared by all other flow cases, but still exhibits the opposite Re-trend, i.e. it increases with increasing Re_θ, something that can also be observed in the simulations by Khujadze & Oberlack (2007), which were similarly tripped at a high Re. This confirms the conclusion drawn in Schlatter & Örlü (2010), that 'the necessary inflow

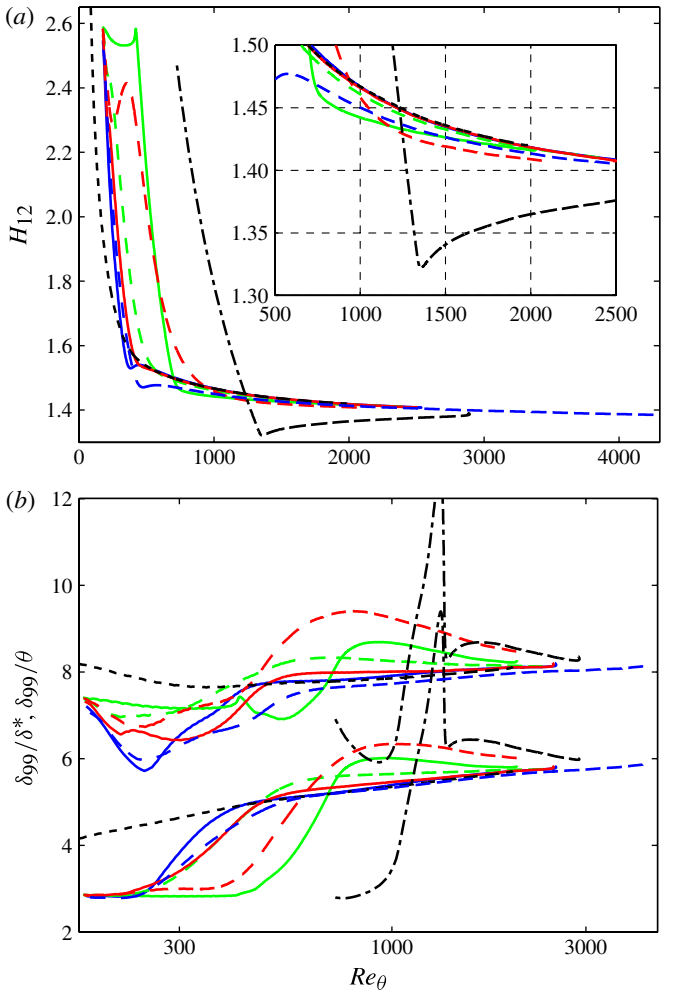

FIGURE 6. (Colour online) Ratios of boundary-layer thicknesses. (*a*) Shape factor, H_{12}, and (*b*) displacement thickness, δ^*, and momentum-loss thickness, θ, over boundary-layer thickness, δ_{99}, as a function of Reynolds number, Re_θ, for various types of tripping. For the meaning of the line styles in this and subsequent figures, see table 1.

length for developed turbulence at higher Re is longer' and emphasizes that tripping at relatively high Re (while at first glance being a cost-efficient method to reach high Re_θ) does not imply that the simulated flow case represents a canonical ZPG TBL flow, not even at a considerably higher $Re_\theta \approx 2900$ considerably downstream of the tripping location. This effect can also be observed in the very recent large-scale DNS by Sillero *et al.* (2011) reaching up to $Re_\theta = 6650$ in which the shape factor appears to be slightly lower than the one predicted by Monkewitz, Chauhan & Nagib (2007) based on experiments or foreseen through the high-Re simulation of Schlatter & Örlü (2010); nevertheless H_{12} approaches the common trend towards the more downstream parts of their simulation box. In consequence, Sillero *et al.* (2011) introduce an accommodation length $\tilde{x}$ related to the convection of structures during their turnover time, which is especially important for the convergence of the largest fluctuations. This length, scaled

by the local boundary thickness, increases with Re_θ, making simulations with inflow positions further downstream gradually more expensive.

A more sensitive measure of the growth of the boundary layer can be obtained from the boundary-layer thicknesses δ^* and θ themselves, normalized by the 99 % thickness, as shown in figure 6(*b*). In particular, the simulation denoted as 'baseline' indeed turns out to be an accurate basis, since all other simulations eventually converge onto the trend prescribed by it. Also the simulation initiated at a lower Reynolds number, LR, nicely agrees with the baseline case starting from $Re_\theta = 400$. Note that although the high-*Re* DNS (Schlatter & Örlü 2010) appears to be slightly below the baseline simulation, this is mainly caused by a different way of evaluating the integrals which yields differences when considerably different domain heights are used (cf. Schlatter & Örlü 2010). Comparing the data in figure 6(*b*) and the collection of DNS data in figure 1(*b*), shows that most literature simulations actually overpredict the two ratios δ_{99}/δ^* and δ_{99}/θ, and seem to show a decreasing trend for low Re_θ followed by a slow increase for higher Re_θ. The present simulations indicate that such an overprediction and change of *Re*-trend is in fact due to a flow that has not sufficiently settled at low Reynolds numbers, which might also be the case for at least some of the literature data collected in table 1. In that regard it is interesting to see that the only truly periodic (and thus fully developed) simulation by Spalart (1988*b*) shows the same increasing trend for both quantities at all Re_θ.

The skin-friction coefficient c_f for the present simulations is depicted in figure 7(*a*) and clearly shows that for all simulations the inflow is laminar (i.e. $c_{f,lam} \approx 0.441 Re_\theta^{-1}$ from the Blasius solution). Depending on tripping, laminar–turbulent transition is induced at different Re_θ, and all except the LF and LA cases exhibit typical overshoots of c_f as a result of transition, after which they settle on a common c_f distribution indicating a rather quick adaptation of the near-wall turbulence. The very different behaviours of the simulations in the region $Re_\theta = 200$–1000 is of course due to the transition mechanism; cases LA and LF are going through a region with the intermittent appearance of turbulent spots embedded in laminar flow which lead to the characteristic c_f curves with a comparatively slow increase towards the turbulent value, as known from bypass transition (Brandt *et al.* 2004). On the other hand, the friction coefficient pertaining to case TS remains essentially at its laminar value during the slow exponential growth of the TS-waves, and shows a sharp increase when the secondary instability takes over. As apparent from the trends in the shape factor and skin-friction distributions, the baseline simulation, the LA, HF and LR cases, as well as the high-*Re* simulation adapt to the turbulent distributions for $Re_\theta < 700$, which again underlines that most of the simulations presented here relate closely to the cases in the experimental counterpart study by Erm & Joubert (1991) and other experimental investigations (Murlis, Tsai & Bradshaw 1982).

The root mean square (r.m.s.) value of wall shear stress ($\tau^+_{w,rms}$) is shown in figure 7(*b*) and, irrespective of tripping mechanism, the curves also indicate a fast convergence towards the classical value of 0.4 (Alfredsson *et al.* 1988) with a small increase with Reynolds number, coming from the growing influence of the outer spectral peak as recently documented by Örlü & Schlatter (2011). It is interesting to point out that even when including the HR case the difference in $\tau^+_{w,rms}$ between all cases is within 2 %, thereby making the DNS by Wu & Moin (2009*a*, 2010) with more than 10 % higher values (irrespective of *Re*) appear quite different from all simulations presented here (see also the discussion in Örlü & Schlatter 2011).

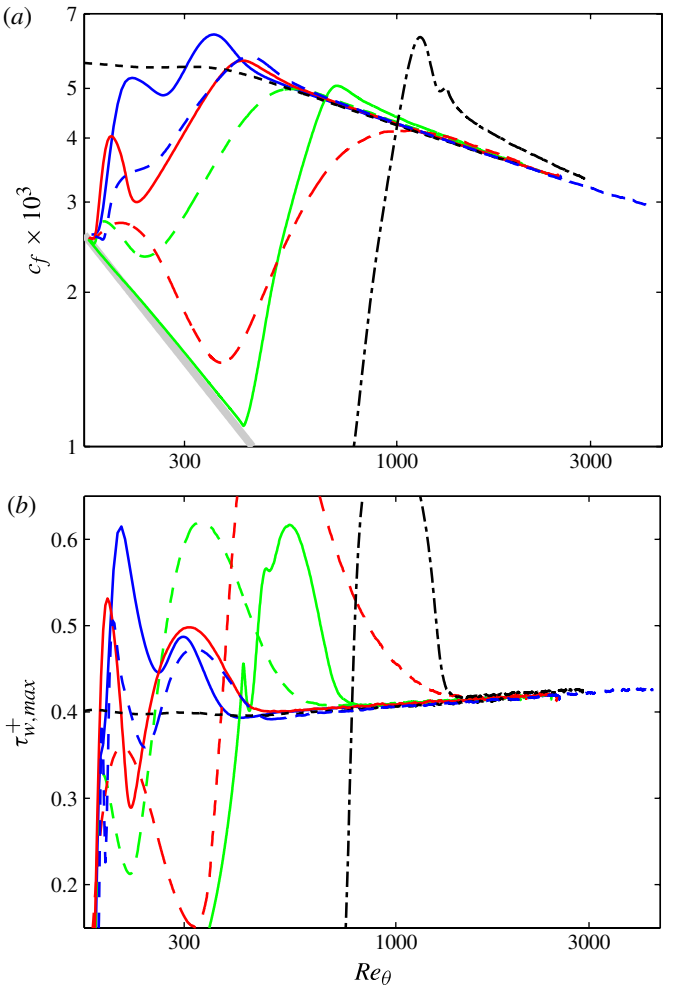

FIGURE 7. (Colour online) (*a*) Skin friction factor, c_f, and (*b*) fluctuating magnitude of the wall-shear stress, $\tau^+_{w,rms}$, as a function of Reynolds number, Re_θ. The thick grey line indicates the laminar (Blasius) skin friction.

3.2. *Mean velocity profiles*

In order to highlight small but significant and important differences in the mean velocity profiles within the inner region it is customary to consider the velocity gradient in terms of the so-called Kármán measure or log-law indicator function (Spalart 1988*b*), since depicting the mean velocity profile in conventional inner scaling will barely expose subtle differences. The log-law indicator function $\Xi = y^+ \,\mathrm{d}U^+/\mathrm{d}y^+$, which is commonly employed to measure the von Kármán constant, κ, in the overlap region (Österlund *et al.* 2000), since it asymptotes to κ^{-1} in a logarithmic region, is presented in figure 8. The four subfigures show curves clustered around distinct Reynolds numbers $Re_\theta = 670, 1100, 1550,$ and 2000. Note that the profiles for the TS, LF and LR cases are not shown for $Re_\theta = 2000$, since these cases might already be affected by the outflow conditions. Additionally, the DNS data by Simens *et al.* (2009), who employ a rescaling and recycling method and thereby avoid the simulation of laminar–turbulent transition, are included as well in figure 8(*b–d*). It is apparent

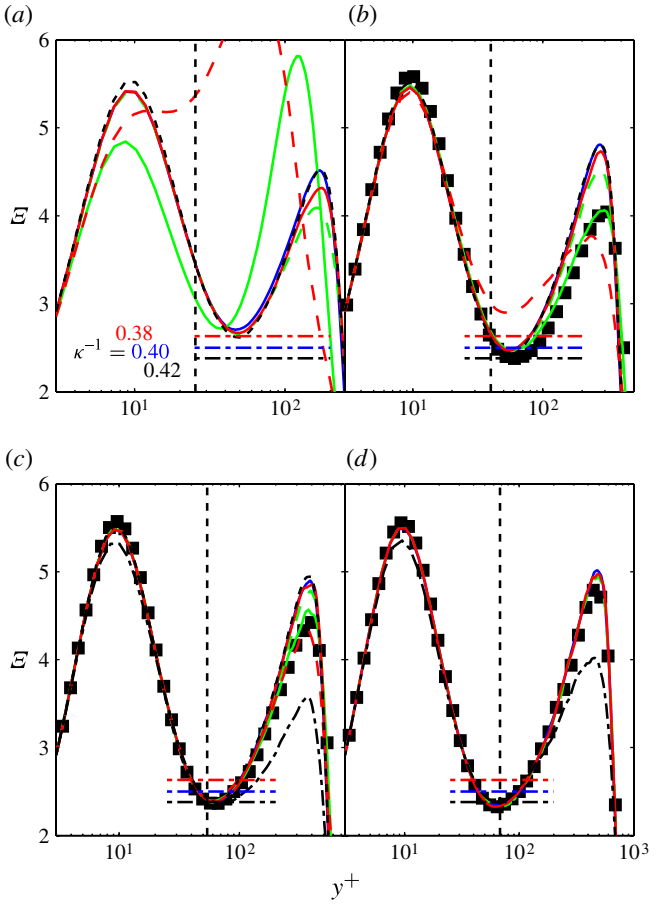

FIGURE 8. (Colour online) Profiles of the indicator function ($\Xi = y^+ \mathrm{d}U^+/\mathrm{d}y^+$ versus y^+) in the inner region of the ZPG TBL flow. Dashed vertical lines indicate the upper boundary of the overlap region, i.e. $y^+/Re_\tau = 0.2$. Profiles are grouped according to their Reynolds number: (*a*) $Re_\theta = 670$; (*b*) $Re_\theta = 1100$; (*c*) $Re_\theta = 1550$; (*d*) $Re_\theta = 2000$. Horizontal lines indicate the levels corresponding to $\kappa^{-1} = 0.38$, 0.40, and 0.42. Data by Simens *et al.* (2009) at around the same Re_θ are depicted as black squares; only a reduced number of interpolated data points is shown in order to ease readability.

that the curves for Ξ within the inner region, i.e. the region below $y^+ \approx 0.2\delta^+$ (indicated by the dashed vertical lines), show a good agreement for all data from $Re_\theta = 1100$ onwards; only the LF case requires a longer development length in accordance with the slower convergence as already discussed with regard to integral quantities.

Although the highest Reynolds number considered here is far from being sufficient to reach an asymptotic logarithmic region or even deduce an accurate value for the log-law constants, the collection of profiles follows the general trend of the composite profile proposed by Monkewitz *et al.* (2007). An exception in this respect is the HR case which exhibits a considerably lower peak value at $y^+ \approx 10$. This is probably not related to its lower numerical resolution since the LR case has the same grid spacing and agrees well with the main body of DNS cases. Hence, it can be concluded that tripping at a considerably high Reynolds number leaves its imprints even within

the inner region of the streamwise mean velocity profile despite a comparatively long development length, a trend that also does not vanish towards the end of the simulation domain, i.e. $Re_\theta = 2900$.

Focusing now on the outer region, i.e. the secondary peak located at $\sim 0.7\delta_{99}^+$, the baseline simulation and cases HF and LR have already reached a value of ~ 4.8 at $Re_\theta = 1100$, whereas the data pertaining to cases still undergoing transition show considerably lower values of around 4. Gradually, all simulations converge and at $Re_\theta = 2000$ most differences have vanished, except for case HR, which is clearly not fully developed at this Re_θ. At this point it is interesting to note that the profile by Simens *et al.* (2009) follows surprisingly closely the TS case for all Re_θ, even though the latter case is going through transition very late and reaches a first turbulent state only at $Re_\theta = 1100$.

The excellent agreement of the velocity gradients (an exception being the HR case), however, does not imply that the velocity profiles agree. This can especially be evinced when considering the deviation of the mean velocity profile from a reference profile (such as the log-law or, as done here, the composite profile description by Chauhan *et al.* 2009) as depicted in figure 9. While there exist considerable differences for the compilation around $Re_\theta = 670$, owing to the different development lengths needed to initiate and in particular complete laminar–turbulent transition, all profiles agree within $\pm 0.025u_\tau$ (u_τ denoting the friction velocity) at the latest at $Re_\theta = 1550$, an exception being again the HR case. Interestingly, the latter case deviates by up to $0.2u_\tau$ from the other cases and follows closely the trend of the DNS by Khujadze & Oberlack (2007), which was tripped at a considerably higher Re as well. This incorrect behaviour is still present at the end of the simulation domain of the HR case (as for the DNS by Khujadze & Oberlack 2007), i.e. at $Re_\theta \approx 2800$. Also included in the compilation are the profiles from the DNS by Simens *et al.* (2009) and Wu & Moin (2010) for comparison. The profiles underline the conclusions already deduced from the integral quantities, i.e. that the near-wall turbulence convergences rapidly, and that with increasing Re the curves within the inner layer not only agree with each other, but also collapse onto the same curve irrespective of the Reynolds number for a successively larger Re-range, thereby laying the foundation for the law of the wall. On the other hand, in the outer region, much longer inflow lengths are needed to reach similar behaviours at a given Reynolds number; for the given data a good agreement is reached at $Re_\theta = 2000$ and higher (excluding case HR for reasons discussed previously).

It might seem an exaggeration to highlight and scrutinize the differences in the mean velocity profiles in such detail as done in figure 9; however, it should be kept in mind that these differences penetrate into the viscous sublayer. There, the observed differences are not negligible when recalling that DNS data are often utilized to validate scaling laws and determine the related constants or parameters in the near-wall region, be it for the mean velocity profile (Durst *et al.* 1996; Örlü, Fransson & Alfredsson 2010) or higher-order moments (Buschmann, Indinger & Gad-el-Hak 2009; Buschmann & Gad-el-Hak 2010). In particular experimentalists have been exploiting near-wall data from mainly DNS or correlations based on them, for instance, to extract the wall skin friction (Kendall & Koochesfahani 2008; Alfredsson, Örlü & Schlatter 2011) or determine the wall position in experimental investigations (Örlü *et al.* 2010; Alfredsson *et al.* 2011) as well as to propose refined Pitot tube corrections for turbulent flows near walls (McKeon *et al.* 2003).

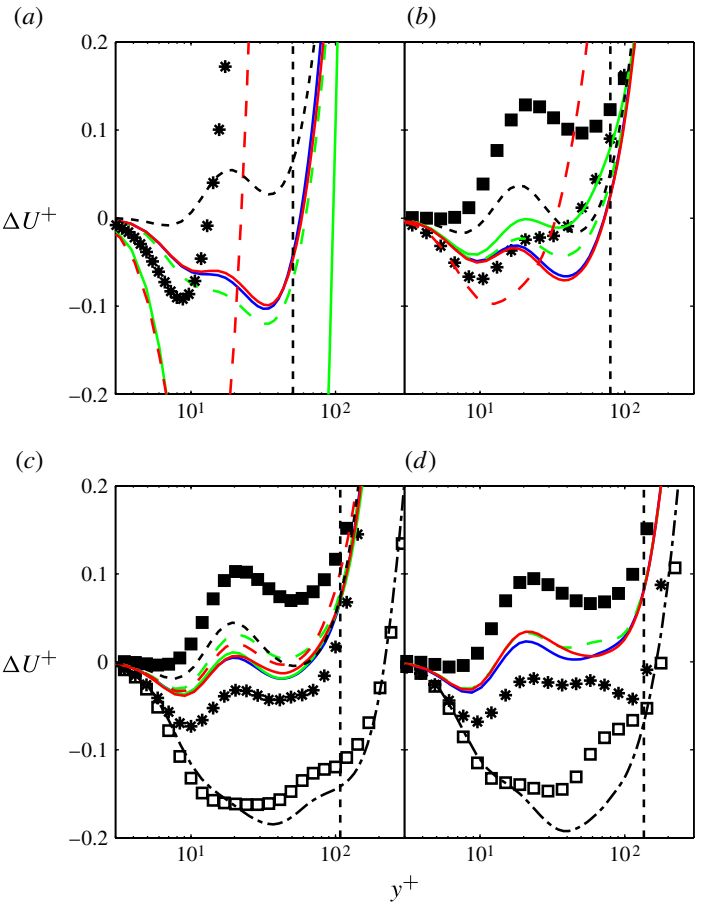

FIGURE 9. (Colour online) Deviation of the inner-scaled mean velocity profile from the modified Musker profile (Chauhan *et al.* 2009) in the inner region of the ZPG TBL flow. Dashed vertical lines indicate the wall-normal boundary of the overlap region, i.e. $y^+/Re_\tau = 0.2$. Profiles are grouped according to their Reynolds number: (*a*) $Re_\theta = 670$; (*b*) $Re_\theta = 1100$; (*c*) $Re_\theta = 1550$; (*d*) $Re_\theta = 2000$. Data by Wu & Moin (2010) ($Re_\theta = 670, 1000, 1410, 1840$, stars), Simens *et al.* (2009) ($Re_\theta = 1100, 1550, 1968$, black squares) and Khujadze & Oberlack (2007) ($Re_\theta = 1663, 2055$, open squares) are depicted as well; note that only a reduced number of interpolated data points is shown in order to ease readability.

3.3. *Inner- and outer-layer convergence*

All of the previous figures clearly indicate a consistent trend in terms of convergence towards a general quantitative behaviour, which essentially follows the trend prescribed by the baseline simulation by Schlatter *et al.* (2009). The topic of inner- and outer-layer convergence has so far been discussed in terms of integral and global quantities as well as the streamwise mean velocity profile. In order to generalize the conclusions on convergence into a general trend at a fixed Reynolds number, i.e. independence of upstream effects, it is natural to consider higher-order moments, and in particular the streamwise velocity r.m.s. profile. To ease the assessment of convergence at both different wall-normal positions and Reynolds numbers, contours

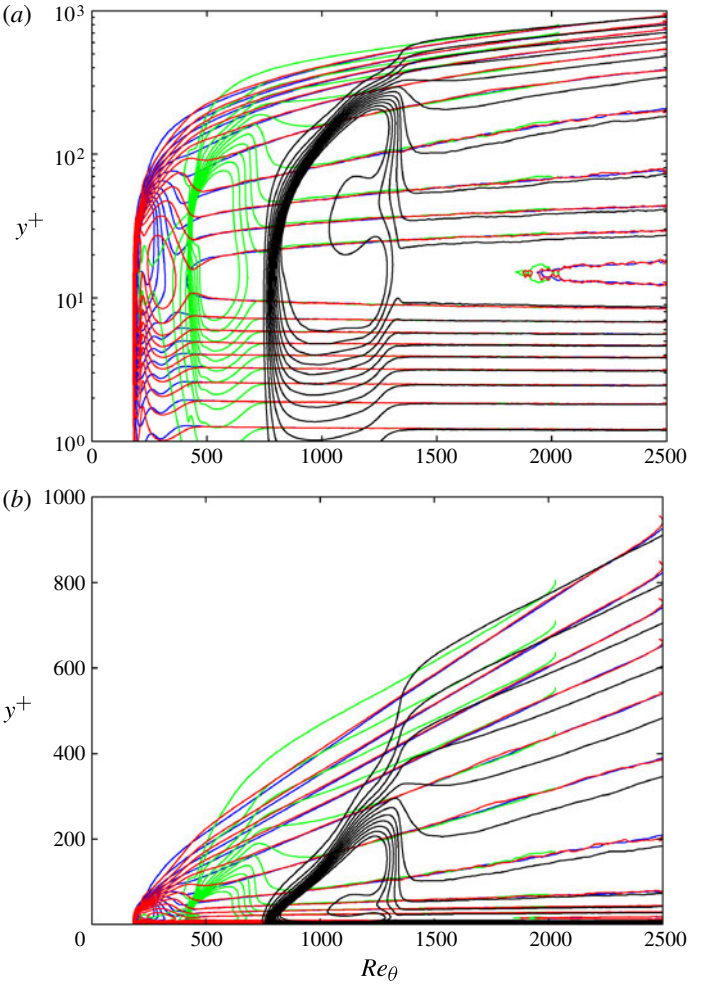

FIGURE 10. Contours of constant root-mean-square values (in steps of $\Delta u^+_{rms} = 0.25$) of the streamwise velocity fluctuations u^+_{rms} as a function of Reynolds number in inner scaling against an (*a*) logarithmic and (*b*) linear ordinate. For clarity only the baseline (blue), TS (green), HF (red), and HR (black) cases are shown.

of u^+_{rms} in a streamwise/wall-normal plane are depicted in figure 10 against both a linear and a logarithmic wall-normal axis in order to enhance the inner and outer layer, respectively. For clarity only the TS, HF and HR cases are shown here in addition to the baseline simulation, where – when excluding the HR case – the TS case exhibits the largest discrepancy, i.e. the slowest convergence. Focusing on the near-wall region (highlighted in the semi-logarithmic representation) in figure 10(*a*) a collapse of the contour lines beyond the near-wall peak of the r.m.s. profile ($y^+ \approx 15$) covering the entire inner region of the boundary layer can be observed for $Re_\theta \geqslant 1000$, indicating that inner-layer convergence is rather quickly obtained. This perception also goes along, both qualitatively and quantitatively, with the short development length for converged statistics in terms of the skin-friction coefficient or the magnitude of the fluctuating wall shear stress apparent from figure 7.

For the outer layer, as shown in figure 10(*b*), the TS case represents the slowest convergence: only for $Re_\theta > 2000$ has the flow forgotten its history and the outer layer reached a common trend prescribed by the baseline simulation and approached by all other (not shown) cases. The general behaviour of an unconverged turbulent flow is that the boundary layer appears to be too thick (in inner units). This is consistent with the scaled boundary-layer thickness δ_{99} shown in figures 1 and 6. Note that even at the end of the simulation domain the HR case has not yet reached the common trend, thereby indicating that tripping at considerably high Re is indeed not a cost-efficient way to obtain data from a fully developed ZPG TBL flow, as already apparent from the differences observed in the mean velocity profile. These observations go along with the conclusions drawn from the shape factor, shown in figure 6, and should be kept in mind when considering DNS (even in long simulation boxes) that were initiated at a high Re (Sillero *et al.* 2011), as well as LES with equivalent approaches (Inoue & Pullin 2011).

An interesting observation with respect to the HR case is that, while convergence is not reached for the shape factor or the skin-friction coefficient nor for the mean and r.m.s. profiles in the inner and outer layers, only the viscous sublayer seems to exhibit convergence. This is particularly emphasized when considering the magnitude of the wall shear stress fluctuations (see figure 7*b*), which even for the HR case converges onto the general trend prescribed by all other simulations. This makes it in particular difficult to explain the considerably higher $\tau^+_{w,rms}$ values obtained in the DNS by Wu & Moin (2009*a*, 2010) (see also discussion in Örlü & Schlatter 2011).

The reminiscence of upstream and history effects within the outer region of the TBL and the related slow convergence of the same quantities can also be observed in the classical representations of mean and r.m.s. profiles depicted in figure 11 for all simulations at $Re_\theta = 1100$ and 2000. While the law of the wall has clearly been established in the streamwise mean velocity profile and the r.m.s. profile collapses (slightly Re-dependent as is well-known) onto a single curve within the inner region, the outer region exhibits remarkable differences in the wake region and considerably differing fluctuation levels. The general trend is, as already stated above, that unconverged flows tend to display a thicker boundary layer. It is, however, gratifying that if transition is initiated at a low enough $Re_\theta < 300$, all streamwise velocity statistics agree well for both inner and outer layer for $Re_\theta > 2000$, an exception being the HR case. It is also worth noting in this respect that the above statement applies to higher-order statistics of the streamwise velocity fluctuations, such as skewness and flatness factors (not shown here), alike. These deductions confirm the experimental conclusions by Erm & Joubert (1991), that noticeable differences for low Reynolds numbers would eventually diminish and that for $Re_\theta \approx 2175$ and above, the data for their three different tested tripping devices agree closely. Similar observations in the range $700 < Re_\theta < 5300$ have also been made by Castillo & Johansson (2002) who found, that 'no effect on the mean velocity profiles or the longitudinal Reynolds normal stress could be seen'. Note in this respect, that no attempt is being made to investigate Reynolds-number effects in mean or streamwise velocity r.m.s. profiles, since the primary goal of the present study is to establish whether or not profiles of statistical quantities agree at a high enough and fixed Reynolds number onto a common, i.e. universal, profile, or whether upstream and initial conditions will prevent universality.

The results shown so far indicate that even low-order statistics, such as integral quantities, mean and fluctuation profiles, exhibit a considerable dependence on the upstream history, at least up to $Re_\theta < 2000$. This finding, although perhaps

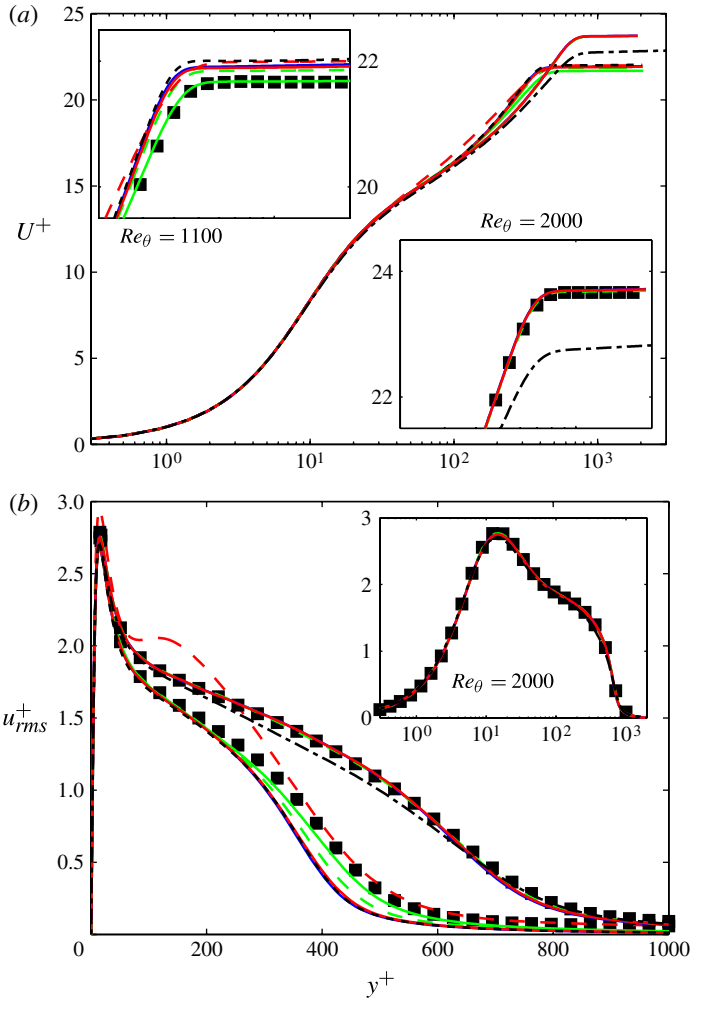

FIGURE 11. (Colour online) (*a*) Streamwise mean velocity profile in inner scaling for $Re_\theta = 1100$ and 2000 with insets showing enlarged wake region from $y^+ = 100$ to 2000. (*b*) Streamwise velocity root-mean-square values for $Re_\theta = 1100$ and 2000 with inset depicting the $Re_\theta = 2000$ case against a logarithmic abscissa. Data by Simens *et al.* (2009) at around the same Re_θ are also depicted; note that only some of the data points are shown in order to ease readability.

expected to some extent, has important consequences, in particular in the light of comparing various DNS data sets among each other and also DNS and experiment with each other. Clearly, such comparisons at lower Reynolds numbers need to be considered with reservations in order to exclude effects simply stemming from different upstream conditions. Also, the present results give some guidelines for what really can be expected in terms of level of agreement for a comparison at lower Re_θ, based on physical reasoning. This in turn is important when compiling databases with individual data to be 'carefully selected' (Buschmann & Gad-el-Hak 2010), or if DNS is to be in 'excellent agreement' (Araya, Jansen & Castillo 2009) with other data.

3.4. *Reynolds stresses and total shear stress*

Within the range of parameters of our diverse types of tripping, the view put forward by Castillo & Johansson (2002) can be assessed with rigour, i.e. that 'neither the profiles of the wall-normal Reynolds stress nor those of the Reynolds shear stress collapsed, thus showing the effects of the upstream conditions' ... 'when the upstream conditions were changed and the local Reynolds number was held constant'. While the above statement resulted from experiments performed in the range $761 < Re_\theta < 5321$, experiments at higher Reynolds numbers let the same principle authors conclude (Seo *et al.* 2004) 'that the upstream conditions affect the profiles at low Reynolds number (i.e. $Re_\theta < 5000$) and its influence attenuates with increasing Reynolds number'. Their conclusion for the wall-normal stress remained intact, in fact it 'showed the strongest dependence on the upstream conditions even for the high Reynolds number data' (Seo *et al.* 2004). It is important to note that in our study turbulence is always induced at the wall, and that cases with severe under- or overstimulation have not been simulated. In particular the latter situation might appear in wind tunnels operating at high speeds. However, these are extreme situations which should be avoided, both experimentally and numerically.

To assess the validity of the aforementioned conjecture based on the present simulation data, profiles of the Reynolds shear stress, $-uv^+$, and the total shear stress, $\mathrm{d}U^+/\mathrm{d}y^+ - uv^+$, are presented in figure 12. It becomes apparent that the $-uv^+$ distributions for the various simulations quickly converge onto a common profile, already attained at $Re_\theta = 1100$. This is in agreement with the previously observed early inner-layer convergence, established e.g. through figures 7 and 10(*a*). To check whether the Reynolds shear stress converges in the outer layer as well, $-uv^+$ is plotted on a linear abscissa in figure 13(*a*) for the same data compilation as in figure 11. In accordance with the picture for the r.m.s. profile, differences at $Re_\theta = 1100$ between the various cases, with the TS case being again closest to the profile by Simens *et al.* (2009), have diminished before reaching $Re_\theta = 2000$. In fact, the Reynolds shear stress profiles depict excellent agreement (excluding again for obvious reasons the HR case), which goes beyond that observed in the streamwise r.m.s. profile depicted in figure 11(*b*). This observation seems not to be in agreement with the conclusions by Castillo & Johansson (2002) and Seo *et al.* (2004). Their statement that the wall-normal component of the Reynolds normal stress 'showed the strongest dependence on the upstream conditions' (Seo *et al.* 2004) can also not be supported through the present data (see figure 13*b*). Although the agreement is not as good as for the Reynolds shear stress, it is certainly comparable to that observed in the streamwise r.m.s. profiles.

Another topic of recent interest is related to the observed overshoot of the total shear stress $\mathrm{d}U^+/\mathrm{d}y^+ - uv^+$ over the wall shear stress $\mathrm{d}U^+/\mathrm{d}y^+|_{y=0}$. This behaviour is clearly visible for the TS and LF cases at $Re_\theta = 670$ depicted in figure 12. Both of these cases were also found to exhibit a relatively slower convergence onto the general trend in all of the shown integral and global quantities, highlighting that this feature is mainly related to an extended transitional zone. However, such an overshoot of the averaged total shear stress over the averaged wall value was also noted in the DNS of a ZPG TBL by Wu & Moin (2009*a*) covering the range $80 \leqslant Re_\theta \leqslant 940$ for which transition is assumed to be completed at $Re_\theta = 750$. Based on the observed gradual decrease of the overshoot with higher Re_θ, the authors conclude that the 'observed total shear stress overshoot in the turbulent region is a diminishing effect of transition, and is unlikely to persist in fully developed turbulent boundary layers' (Wu & Moin 2009*a*). However, in a follow-up study by Wu (2010) the total stress overshoot present

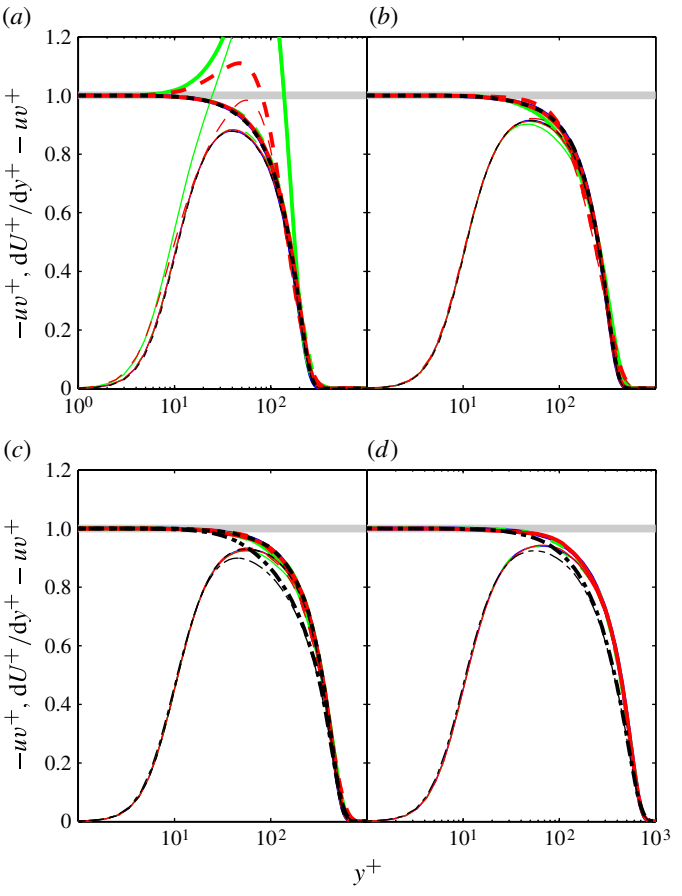

FIGURE 12. (Colour online) Reynolds shear stress, uv^+, and total shear stress, $\mathrm{d}U^+/\mathrm{d}y^+ - uv^+$, denoted as thin and thick lines, respectively. The profiles are grouped according to their Reynolds number: (*a*) $Re_\theta = 670$; (*b*) $Re_\theta = 1100$; (*c*) $Re_\theta = 1550$; (*d*) $Re_\theta = 2000$.

in the data by Wu & Moin (2010), which extends the previous DNS up to $Re_\theta = 1950$, was associated with a localized streamwise acceleration of the streamwise velocity component in the transitional region and deemed 'valid, and presumably general to a class of similar types of boundary layers' (Wu 2010). In fact, the strength of the overshoot in the total shear stress present in the data by Wu & Moin (2010) was found to gradually decrease from around 10 % down to around 2 % until $Re_\theta = 900$. From there on it remained constant at a level of 2 % up to their highest Re_θ as apparent from the profile shown in figure 14 at $Re_\theta = 1840$ or the profile in the inset of figure 15. To further study this phenomenon, a close-up of figure 12 is presented in figure 14, comparing our data with those by Simens *et al.* (2009) and Wu & Moin (2010). Interestingly, Wu (2010) denotes the upper end of the Reynolds number region as turbulent when it comes to the 'preponderance of hairpin vortices in the turbulent boundary-layer region up to $Re_\theta = 1850$' (Wu 2010). This so-called 'forest of hairpins' (Wu & Moin 2009*b*) has received considerable attention and is controversially debated (see e.g. discussions in Marusic 2009; Gad-el-Hak 2009; Jiménez *et al.* 2010; Schlatter *et al.* 2010*a*), although Schlatter *et al.* (2010*a*) have shown that at 'higher *Re*

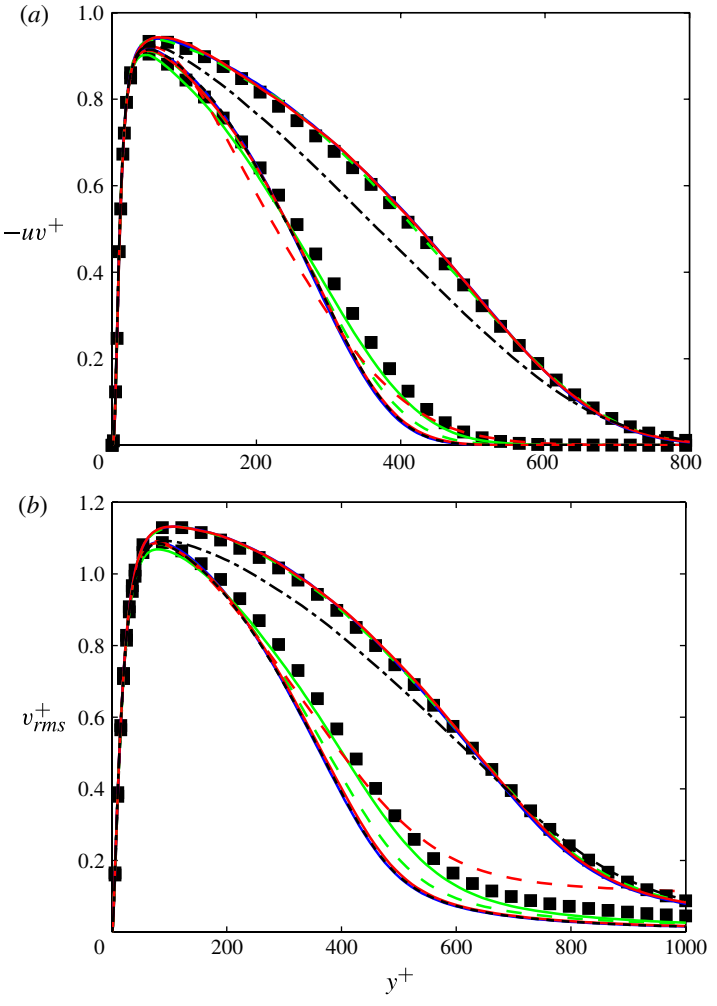

FIGURE 13. (Colour online) (*a*) Reynolds shear stress and (*b*) wall-normal velocity root mean square, v^+_{rms}, value as a function of Reynolds number for $Re_\theta = 1100$ and 2000 together with data by Simens *et al.* (2009) ($Re_\theta = 1100, 1968$) (symbols). Note that only a fraction of the available data points is shown in order to ease readability.

(say $Re_\theta > 2000$) these structures are no longer seen as being dominant; the coherence is clearly lost, both in the near-wall region as well as in the outer layer of the boundary layer'.

For all the present simulated cases, irrespective of tripping mechanism, the overshoot of the averaged total shear stress over the averaged wall shear stress is vanishing in the turbulent region (up to 0.01 %). The overshoot is thus clearly associated with laminar–turbulent transition in accordance with previous transition studies (for instance in the data by Brandt *et al.* 2004). This becomes clear from figure 15 which shows the streamwise evolution of the maximum total stress. For $Re_\theta \geqslant 1100$, where the inner-layer convergence has been established for all simulations (excluding again case HR), none of the simulated cases exhibits values larger than unity in the total shear stress. This observation also extends to most of the other DNS

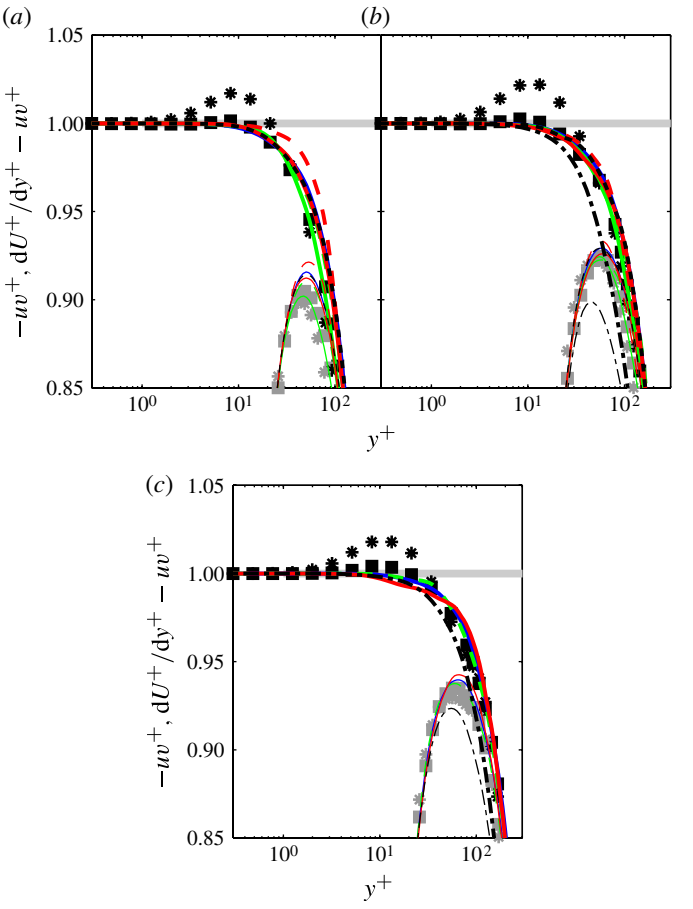

FIGURE 14. (Colour online) Close-up of figure 12 for: (*a*) $Re_\theta = 1100$; (*b*) $Re_\theta = 1550$; (*c*) $Re_\theta = 2000$. Also shown are data by Wu & Moin (2010) ($Re_\theta = 1000, 1410, 1840$) and Simens *et al.* (2009) ($Re_\theta = 1100, 1550, 1968$) with grey symbols denoting the Reynolds shear stress; note that only some of the data points are shown in order to ease readability.

of ZPG TBL flows compiled in table 1, only the data by Simens *et al.* (2009) showing a minor overshoot of $\tau_{tot}^+ \approx 0.4\,\%$. It remains therefore unclear why the data by Wu & Moin (2010) show such an overshoot well into the turbulent region. A residual effect of a pressure gradient is certainly possible; however based on the available data this remains a speculation. Also, an effect of ambient free-stream turbulence might be possible too, but has not been observed in other cases involving bypass transition, as we confirmed by postprocessing the data by Schlatter *et al.* (2010*b*). We can thus state that, based on our data, such an overshoot is not a property of a canonical turbulent boundary layer. Similarly, in fully developed channel flows, the total shear stress distribution is linear, and no overshoot is possible.

4. Summary and conclusions

The recent assessment of a compilation of DNS data pertaining to canonical zero-pressure-gradient turbulent boundary layers by Schlatter & Örlü (2010) showed

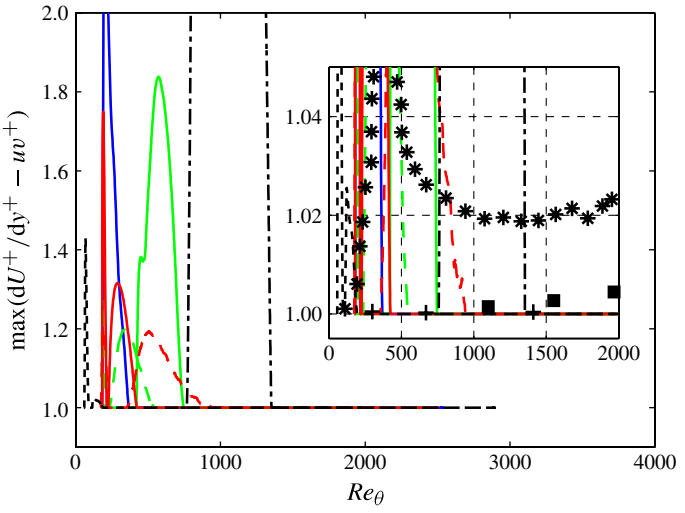

FIGURE 15. (Colour online) Wall-normal maximum of the total shear stress, $\max(dU^+/dy^+ - uv^+)$, for all cases, including data by Spalart (1988*b*), Simens *et al.* (2009) and Wu & Moin (2010) (see inset); note that not all data points by Wu & Moin (2010) are shown in order to ease readability.

surprisingly large differences between the individual data sets, not only in the skin-friction coefficient c_f or shape factor H_{12}, but also in their predictions of mean and fluctuation profiles far into the sublayer. The main difference between these simulations has been the way turbulence is introduced into the domain, a problem which can be avoided in parallel flows (pipes and channels) by assuming periodicity. Thus, by re-simulating the DNS setup by Schlatter *et al.* (2009), but with a number of physically different inflow conditions and tripping effects, the downstream evolution of integral and global quantities as well as mean and fluctuation profiles is analysed in the present contribution. Based on these new results, which can be considered a DNS counterpart of the seminal study by Erm & Joubert (1991), inflow and tripping effects in a boundary layer can now be quantified. It is reasonable to conclude that the memory of transitional effects over the entire boundary-layer height as well as the slow convergence of the outer layer are the main factors explaining a large part of the differences observed by Schlatter & Örlü (2010). Although it remains an open question how to strictly define conditions to apply to determine whether a boundary layer has reached a 'fully-turbulent' or 'canonical' state, it becomes clear from the present data that neither the shape factor nor the skin-friction coefficient alone are sufficient. The outer region of the boundary layer, not unexpectedly, requires longer inflow length than the near-wall region. On the other hand, the data presented here provide useful guidance on what accuracy (i.e. level of discrepancy between different cases) might be expected for certain Reynolds numbers, and on what behaviour might be expected for flows that are too close to transition having not yet reached a fully turbulence near-equilibrium state. Based on the comparisons given in the present study, it can further be concluded that the simulation setup by Schlatter *et al.* (2009), employed here as baseline data, indeed constitutes a generic zero-pressure-gradient turbulent boundary layer with minimal upstream dependence and history effects from $Re_\theta \approx 500$ onwards. This is best illustrated in figures 6 and 10 where

the baseline data appear to prescribe the trend onto which all other simulations are converging.

Within the range of tripping types studied in this paper, the present data have also been used to test two hypotheses put forward by Castillo and co-workers (Castillo & Johansson 2002; Seo *et al.* 2004): contrary to their measurements, the wall-normal fluctuations as well as the Reynolds shear stress do collapse for higher Reynolds numbers, more or less in a similar way to the streamwise velocity fluctuations. It can therefore be concluded that – irrespective of the quantity considered, be it of integral nature, mean velocity profiles or higher-order moments of the streamwise velocity component – the Reynolds shear stress and the wall-normal component of the Reynolds normal stress all agree well for both the inner and outer layer for $Re_\theta > 2000$, if transition is initiated inside the boundary layer at a low enough $Re_\theta < 300$, avoiding over- or understimulation of the flow.

This directly implies that for a meaningful comparison between numerical and/or wind tunnel experiments, a Reynolds number $Re_\theta > 2000$ constitutes a lower limit for reaching a fully turbulent state irrespective of transition trigger, provided that transition is initiated early enough, and within reasonable bounds for the tripping characteristics such as amplitude etc. Below that Re_θ transitional, and in particular upstream (since these disappear much more gradually), effects can be detected which are difficult to isolate and quantify. Of course, when employing numerical methods such as recycling or artificial turbulent inflow conditions in DNS, the inflow Reynolds number can be chosen higher, but even then sufficient inflow length must to be provided. Triggering transition at a higher Reynolds number leads to significantly increased inflow length.

Additionally, we have also studied the overshoot of the total shear stress over the wall-limiting value, as a function of tripping parameters and Reynolds number. Interestingly, for our data this overshoot could solely be linked to the transitional region alone, and vanishes quickly. Conversely, the data by Wu & Moin (2010) feature a Reynolds-number-independent overshoot of 2 % from $Re_\theta \approx 900$ up to their highest $Re_\theta = 1850$.

Building upon the present results, a detailed comparison between our recent DNS and experiments on a ZPG TBL flow at $Re_\theta = 2500$ and 4000 by Örlü & Schlatter (2012) yields excellent agreement for integral, statistical as well as structural/spectral quantities. This result clearly demonstrates that in both simulation and experiment the same flow is studied, and that upstream effects could indeed be eliminated sufficiently.

Acknowledgements

Computer time provided by the Swedish National Infrastructure for Computing (SNIC) is gratefully acknowledged. The authors are grateful for all the data made available by the other researchers referenced in the text.

REFERENCES

ALFREDSSON, P. H., JOHANSSON, A. V., HARITONIDIS, J. H. & ECKELMANN, H. 1988 The fluctuating wall-shear stress and the velocity field in the viscous sublayer. *Phys. Fluids* **31**, 1026–1033.

ALFREDSSON, P. H., ÖRLÜ, R. & SCHLATTER, P. 2011 The viscous sublayer revisited – exploiting self-similarity to determine the wall position and friction velocity. *Exp. Fluids* **51**, 271–280.

ARAYA, G., JANSEN, K. & CASTILLO, L. 2009 Inlet condition generation for spatially developing turbulent boundary layers via multiscale similarity. *J. Turbul.* **10** (36), 1–33.

BERTOLOTTI, F. P., HERBERT, T. & SPALART, P. R. 1992 Linear and nonlinear stability of the Blasius boundary layer. *J. Fluid Mech.* **242**, 441–474.

BRANDT, L., SCHLATTER, P. & HENNINGSON, D. S. 2004 Transition in boundary layers subject to free stream turbulence. *J. Fluid Mech.* **517**, 167–198.

BUSCHMANN, M. H. & GAD-EL-HAK, M. 2010 Normal and cross-flow Reynolds stresses: differences between confined and semi-confined flows. *Exp. Fluids* **49**, 213–223.

BUSCHMANN, M. H., INDINGER, T. & GAD-EL-HAK, M. 2009 Near-wall behaviour of turbulent wall-bounded flows. *Intl J. Heat Fluid Flow* **30**, 993–1006.

CASTILLO, L. & JOHANSSON, T. G. 2002 The effects of the upstream conditions on a low Reynolds number turbulent boundary layer with zero pressure-gradient. *J. Turbul.* **3**, 1–19.

CHAUHAN, K. A., MONKEWITZ, P. A. & NAGIB, H. M. 2009 Criteria for assessing experiments in zero pressure-gradient boundary layers. *Fluid Dyn. Res.* **41**, 021404.

CHEVALIER, M., SCHLATTER, P., LUNDBLADH, A. & HENNINGSON, D. S. 2007 SIMSON – A pseudo-spectral solver for incompressible boundary layer flow. *Tech. Rep.* TRITA-MEK 2007:07, Royal Institute of Technology, Stockholm, Sweden.

COLES, D. E. 1954 The problem of the turbulent boundary layer. *Z. Angew. Math. Phys.* **5**, 181–203.

DURST, F., KIKURA, H., LEKAKIS, I., JOVANOVIC, J. & YE, Q. 1996 Wall shear stress determination from near-wall mean velocity data in turbulent pipe and channel flows. *Exp. Fluids* **20**, 417–428.

EMMONS, H. W. 1951 The laminar–turbulent transition in a boundary layer. Part 1. *J. Aero. Sci.* **18**, 490–498.

ERM, L. P. & JOUBERT, P. N. 1991 Low-Reynolds-number turbulent boundary layers. *J. Fluid Mech.* **230**, 1–44.

FERNHOLZ, H. H. & FINLEY, P. J. 1996 The incompressible zero-pressure-gradient turbulent boundary layer: an assessment of the data. *Prog. Aerosp. Sci.* **32**, 245–311.

FERRANTE, A. & ELGHOBASHI, S. E. 2005 Reynolds number effect on drag reduction in a microbubble-laden spatially developing turbulent boundary layer. *J. Fluid Mech.* **543**, 93–106.

GAD-EL-HAK, M. 2009 DNS of turbulent boundary layers: the breakthrough that opened a can of worms. *CFD Lett.* **1** (2), ii–iv.

INOUE, M. & PULLIN, D. I. 2011 Large-eddy simulation of the zero-pressure-gradient turbulent boundary layer up to $Re_\theta = O(10^{12})$. *J. Fluid Mech.* **686**, 507–533.

JEONG, J. & HUSSAIN, F. 1995 On the identification of a vortex. *J. Fluid Mech.* **285**, 69–94.

JIMÉNEZ, J., HOYAS, S., SIMENS, M. P. & MIZUNO, Y. 2010 Turbulent boundary layers and channels at moderate Reynolds numbers. *J. Fluid Mech.* **657**, 335–360.

JIMÉNEZ, J., SIMENS, M. P., HOYAS, S. & MIZUNO, Y. 2008 Entry length requirements for direct simulations of turbulent boundary layers. *Center for Turbulence Research, Annual Research Briefs* 381–390.

KENDALL, A. & KOOCHESFAHANI, M. M. 2008 A method for estimating wall friction in turbulent wall-bounded flows. *Exp. Fluids* **44**, 773–780.

KHUJADZE, G. & OBERLACK, M. 2004 DNS and scaling laws from new symmetry groups of ZPG turbulent boundary layer flow. *Theor. Comput. Fluid Dyn.* **18**, 391–411.

KHUJADZE, G. & OBERLACK, M. 2007 New scaling laws in ZPG turbulent boundary layer flow. In *Proc. 5th Intl Symp. on Turbulence and Shear Flow Phenomena, München, Germany* (ed. R. Friedrich, N. A. Adams, J. K. Eaton, J. A. C. Humphrey, N. Kasagi & M. A. Leschziner).

KIM, J., MOIN, P. & MOSER, R. D. 1987 Turbulence statistics in fully developed channel flow at low Reynolds number. *J. Fluid Mech.* **177**, 133–166.

KLEBANOFF, P. S. & DIEHL, W. S. 1954 Some features of artificially thickened fully developed turbulent boundary layers with zero pressure-gradient. *NACA Tech. Rep.* 1110.

KOMMINAHO, J. & SKOTE, M. 2002 Reynolds stress budgets in couette and boundary layer flows. *Flow Turbul. Combust.* **68**, 167–192.

LANDAHL, M. T. 1980 A note on an algebraic instability of inviscid parallel shear flows. *J. Fluid Mech.* **98**, 243–251.

LEE, J. H. & SUNG, H. J. 2011 Direct numerical simulation of a turbulent boundary layer up to $Re_\theta = 2500$. *Intl J. Heat Fluid Flow* **32**, 1–10.

MARUSIC, I. 2009 Unravelling turbulence near walls. *J. Fluid Mech.* **630**, 1–4.

MARUSIC, I., MCKEON, B. J., MONKEWITZ, P. A., NAGIB, H. M., SMITS, A. J. & SREENIVASAN, K. R. 2010 Wall-bounded turbulent flows at high Reynolds numbers: recent advances and key issues. *Phys. Fluids* **22**, 065103.

MCKEON, B. J., LI, J. D., JIANG, W., MORRISON, J. F. & SMITS, A. J. 2003 Pitot probe corrections in fully developed turbulent pipe flow. *Meas. Sci. Technol.* **14**, 1449–1458.

MONKEWITZ, P. A., CHAUHAN, K. A. & NAGIB, H. M. 2007 Self-consistent high-Reynolds-number asymptotics for zero-pressure-gradient turbulent boundary layers. *Phys. Fluids* **19**, 115101.

MONTY, J. P. & CHONG, M. S. 2009 Turbulent channel flow: comparison of streamwise velocity data from experiments and direct numerical simulation. *J. Fluid Mech.* **633**, 461–474.

MURLIS, J., TSAI, H. & BRADSHAW, P. 1982 The structure of turbulent boundary layers at low Reynolds numbers. *J. Fluid Mech.* **122**, 13–56.

NORDSTRÖM, J., NORDIN, N. & HENNINGSON, D. S. 1999 The fringe region technique and the Fourier method used in the direct numerical simulation of spatially evolving viscous flows. *SIAM J. Sci. Comput.* **20** (4), 1365–1393.

ÖRLÜ, R., FRANSSON, J. H. M. & ALFREDSSON, P. H. 2010 On near wall measurements of wall bounded flows – the necessity of an accurate determination of the wall position. *Prog. Aerosp. Sci.* **46**, 353–387.

ÖRLÜ, R. & SCHLATTER, P. 2011 On the fluctuating wall shear stress in zero pressure-gradient turbulent boundary layer flows. *Phys. Fluids* **23**, 021704.

ÖRLÜ, R. & SCHLATTER, P. 2012 Turbulent boundary layer flow: comparing experiments with DNS. In *Progress in Turbulence and Wind Energy IV*. iTi *Conference, September 19–22 2010* (ed. M. Oberlack, J. Peinke, A. Talamelli, L. Castillo & M. Hölling), pp. 213–216. Springer.

ÖSTERLUND, J. M., JOHANSSON, A. V., NAGIB, H. M. & HITES, M. H. 2000 A note on the overlap region in turbulent boundary layers. *Phys. Fluids* **12**, 1–4.

SCHLATTER, P., CHEVALIER, M., ILAK, M. & HENNINGSON, D. S. 2010*a* The structure of a turbulent boundary layer studied by numerical simulation. Preprint http://arxiv.org/abs/1010.4000.

SCHLATTER, P., DEUSEBIO, E., DE LANGE, R. & BRANDT, L. 2010*b* Numerical study of the stabilisation of boundary-layer disturbances by finite amplitude streaks. *Intl J. Flow Control* **2** (4), 259–288.

SCHLATTER, P., LI, Q., BRETHOUWER, G., JOHANSSON, A. V. & HENNINGSON, D. S. 2010*c* Simulations of spatially evolving turbulent boundary layers up to $Re_\theta = 4300$. *Intl J. Heat Fluid Flow* **31**, 251–261.

SCHLATTER, P. & ÖRLÜ, R. 2010 Assessment of direct numerical simulation data of turbulent boundary layers. *J. Fluid Mech.* **659**, 116–126.

SCHLATTER, P., ÖRLÜ, R., LI, Q., BRETHOUWER, G., FRANSSON, J. H. M., JOHANSSON, A. V., ALFREDSSON, P. H. & HENNINGSON, D. S. 2009 Turbulent boundary layers up to $Re_\theta = 2500$ studied through simulation and experiment. *Phys. Fluids* **21**, 051702.

SEO, J., CASTILLO, L., JOHANSSON, T. G. & HANGAN, H. 2004 Reynolds stress in turbulent boundary layers at high Reynolds number. *J. Turbul.* **5** (15), 1–22.

SILLERO, J., JIMÉNEZ, J., MOSER, R. D. & MALAYA, N. P. 2011 Direct simulation of a zero-pressure-gradient turbulent boundary layer up to $Re_\theta = 6650$. *J. Phys.: Conf. Ser.* **318**, 022023.

SIMENS, M. P., JIMÉNEZ, J., HOYAS, S. & MIZUNO, Y. 2009 A high-resolution code for turbulent boundary layers. *J. Comput. Phys.* **228**, 4218–4231.

SKOTE, M., HARITONIDIS, J. H. & HENNINGSON, D. S. 2002 Varicose instabilities in turbulent boundary layers. *Phys. Fluids* **14**, 2309–2323.

SMITS, A. J., MATHESON, N. & JOUBERT, P. N. 1983 Low-Reynolds-number turbulent boundary layers in zero and favourable pressure-gradients. *J. Ship Res.* **27**, 147–157.

SPALART, P. R. 1988*a* Direct numerical study of leading edge contamination. In *Fluid Dynamics of Three-Dimensional Turbulent Shear Flows and Transition*, *AGARD CP*-438, pp. 5.1–5.13. AGARD.

SPALART, P. R. 1988*b* Direct simulation of a turbulent boundary layer up to R_θ=1410. *J. Fluid Mech.* **187**, 61–98.

WU, X. 2010 Establishing the generality of three phenomena using a boundary layer with free stream passing wakes. *J. Fluid Mech.* **664**, 193–219.

WU, X. & MOIN, P. 2009*a* Direct numerical simulation of turbulence in a nominally zero-pressure-gradient flat-plate boundary layer. *J. Fluid Mech.* **630**, 5–41.

WU, X. & MOIN, P. 2009*b* Forest of hairpins in a low-Reynolds-number zero-pressure-gradient flat-plate boundary layer. *Phys. Fluids* **21**, 091106.

WU, X. & MOIN, P. 2010 Transitional and turbulent boundary layer with heat transfer. *Phys. Fluids* **22**, 085105.